Title

Site-Dependent Fluctuations Optimize Electronic Energy Transfer in the Fenna–Matthews–Olson Protein

Journal

The Journal of Physical Chemistry B, 123(46)

ISSN

1520-6106

Authors

Saito, Shinji
Higashi, Masahiro
Fleming, Graham R

Publication Date

2019-11-21

DOI

10.1021/acs.jpcb.9b07456

Peer reviewed

Site-Dependent Fluctuations Optimize Electronic Energy Transfer in the Fenna–Matthews–Olson Protein

Shinji Saito,[*,†,‡] Masahiro Higashi,[§,∥] and Graham R. Fleming[⊥,#,¶]

[†]Institute for Molecular Science, Myodaiji, Okazaki, Aichi 444-8585, Japan

[‡]The Graduate University for Advanced Studies, Myodaiji, Okazaki, Aichi 444-8585, Japan

[§]Department of Molecular Engineering, Graduate School of Engineering, Kyoto University, Kyoto daigaku-katsura, Nishikyo-ku, Kyoto 615-8510, Kyoto, Japan

[∥]JST, PRESTO, 4-1-8 Honcho, Kawaguchi, Saitama 332-0012, Japan

[⊥]Department of Chemistry, University of California, Berkeley, California 94720, United States

[#]Molecular Biophysics and Integrated Bioimaging Division, Lawrence Berkeley National Lab, Berkeley, California 94720, United States

[¶]Kavli Energy Nanosciences Institute at Berkeley, Berkeley, California 94720, United States

ABSTRACT: Light absorbed by light-harvesting antennae is transferred to the reaction center (RC). The excitation energy transfer (EET) to the RC is known to proceed with nearly perfect quantum yield. However, understanding of EET is still limited at the molecular level. Here, we examine the dynamics in the Fenna–Matthews–Olson (FMO) protein by developing an efficient molecular dynamics simulation that can properly describe the electronic properties of bacteriochlorophylls. We find that the FMO protein consists of sites with heterogeneous fluctuations extending from fast to slow modulation. We also find that efficient EETs are facilitated by site-dependent fluctuations that enhance the resonance condition between neighboring sites with large site energy differences and circumvent exciton trapping on the pathway to the RC. Knowledge of site-dependent fluctuations is an important component of understanding optimization of EET in photosynthetic systems.

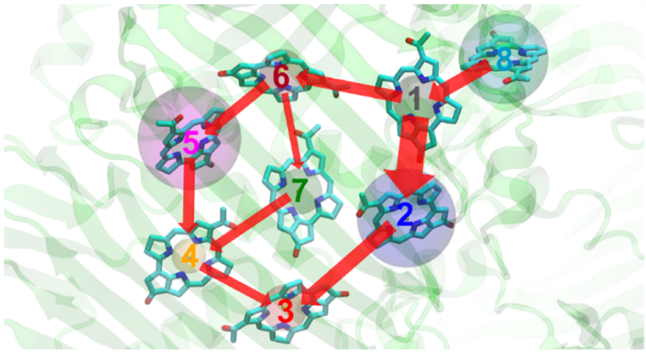

1. INTRODUCTION

Photosynthesis is an essential process for life on Earth which converts light energy to chemical energy through a series of processes.[1,2] These processes have extensively been investigated for the understanding of not only natural photosynthesis but also artificial photosynthesis. The Fenna–Mathews–Olson (FMO) protein of green sulfur bacteria is one of the extensively studied light-harvesting antennae in natural photosynthetic systems. The FMO protein consists of a trimer (Figure 1a). It was initially thought that each subunit binds seven bacteriochlorophyll (BChl) molecules.[3,4] However, later, it was shown that an eighth BChl molecule exists at the interface between subunits (Figure 1b).[5] The FMO protein has gained attention because it is the first protein showing coherent oscillations in pump–probe and two-dimensional electronic spectra[6−8] and is a water-soluble broad-band antenna with nearly perfect quantum efficiency of the excitation energy transfer (EET). Based on various experimental studies, it is considered that the excitation energy is provided from site 3 to the reaction center (RC)[9] and that site 8 is likely to be the acceptor from the chlorosome,[5] though the identification of acceptor is still under debate.

Very high quantum efficiency of EET is observed not only for the FMO protein but also for all light-harvesting photosynthetic proteins. It is therefore crucial to elucidate how such highly efficient EET is realized in proteins. In considering the remarkable efficiency of photosynthetic light-harvesting proteins, a considerable body of work has demonstrated that the spacings, orientations, and site energies of the chromophores can be manipulated by the protein to achieve ultrafast energy transport.[1,2,10,11] The spatial arrangement and site energies determine the strength of the electronic coupling between molecules. However, an equally important quantity in determining the rate of energy transfer is the reorganization energy, or more generally, the spectral density. It has not been possible to determine experimental spectral densities for individual chromophore sites in antenna proteins,

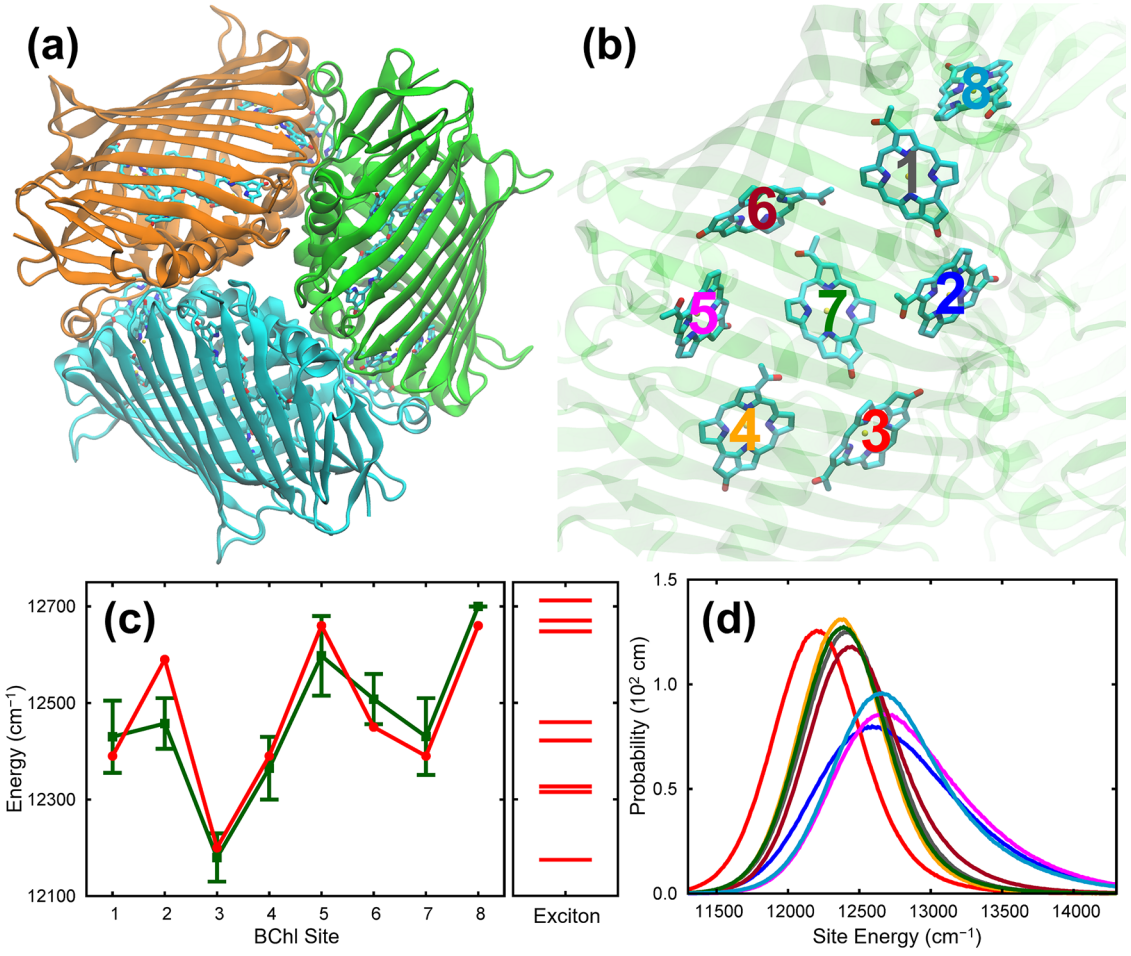

Figure 1. (a) FMO complex trimer. (b) Eight BChl *a* pigments in a monomer subunit of FMO complex. (c) Comparison of the calculated site energies at 300 K (red) with the result fitted to experimental data (green). The calculated site energies correspond to the maxima of the site energy distributions. The experimental data of sites 1−7 correspond to the minimum and maximum of six site energies obtained from the fit to the experimental results,[36−41] whereas only one fitted result is available for site 8.[41] Exciton energy levels at 300 K are also plotted. Exciton energies and the corresponding eigenfunctions are given in Table S1. (d) Site energy distribution of each site calculated from MD simulations at 300 K. The site energy distributions at sites 1, 2, 3, 4, 5, 6, 7, and 8 are shown by gray, blue, red, orange, magenta, brown, green, and sky-blue lines, respectively.

and the question of whether individual site fluctuations are in any way optimized in nature has remained unresolved. Most quantum dynamical models, instead, utilize an identical spectral density for each site in the protein. Recent computational studies have shown the presence of site-dependent fluctuations in the FMO protein.[12−20] Systematic investigations on the origin of efficient EET have not been conducted yet, though the effect of a change of the spectral densities at sites 1 and 2 on EET has been examined.[14]

To understand the mechanism of efficient EET at the molecular level, it is necessary to examine the individual spectral densities which require quantum mechanical (QM) calculations. However, QM calculations, such as QM/molecular mechanical (QM/MM) calculations, demand high computational costs, so that it is impractical to perform long molecular dynamics (MD) simulations with the QM calculation. Thus, in many previous studies, the spectral densities of pigments as well as site energies and excitonic couplings have been calculated with QM/MM calculations at configurations obtained from MD simulations with MM force fields.

However, there are at least two problems to be addressed in the method with a combination of QM/MM calculations and MD simulations.[14,17] One is the accuracy of the QM calculations and the other is the difference between the ground-state energy landscapes of a pigment calculated from QM calculations and MD simulations. For the first problem, we found the importance of the careful determination of the so-called range-separated parameter in time-dependent density functional theory (TDDFT) calculation.[17] The second problem arises from the difference between the descriptions of pigment in the ground state by QM calculations and MD simulations. To overcome the second problem, Coker and his co-workers have separated the spectral densities into intra- and intermolecular contributions: the intermolecular contribution is evaluated with the MD simulation, whereas the intramolecular contribution is obtained from the QM/MM normal mode analysis at optimized geometry.[14,18] We developed the molecular mechanics with the Shepard interpolation correction (MMSIC) method, which can accurately and efficiently reproduce global potential energy surface of all the BChl molecules in the FMO protein covered by MD simulations.[17] Kim and Rhee have also constructed an interpolated potential energy function of BChl *a* pigment using 1500 data points.[19,20]

In this study, by further developing an accurate and efficient method for the calculation of excitonic couplings, we enable to

not only reproduce existing experimental results, such as site energies, spectral density, and absorption spectra, but also elucidate the detailed site-dependent fluctuations of BChl molecules in the FMO protein. As a result, we reveal the role of individual site fluctuations in the efficient EET in the FMO complex of green sulfur bacteria.

2. THEORETICAL METHODS

2.1. MMSIC Method. The details of the MMSIC method are found in our previous study.[17] Here we summarize them only briefly. In QM/MM calculations, the total QM/MM energy of a system is expressed as

$$\begin{aligned} V^{\mathrm{QM/MM}}(\mathbf{R}, \mathbf{R}^{\mathrm{MM}}) &= V^{\mathrm{QM}}(\mathbf{R}, \mathbf{R}^{\mathrm{MM}}) + V^{\mathrm{QM\text{-}MM}}(\mathbf{R}, \mathbf{R}^{\mathrm{MM}}) \\ &\quad + V^{\mathrm{MM}}(\mathbf{R}^{\mathrm{MM}}) \\ &= V^{\mathrm{QM}}(\mathbf{R}, \mathbf{R}^{\mathrm{MM}}) + V_{\mathrm{ES}}^{\mathrm{QM\text{-}MM}}(\mathbf{R}, \mathbf{R}^{\mathrm{MM}}) \\ &\quad + V_{\mathrm{non\text{-}ES}}^{\mathrm{QM\text{-}MM}}(\mathbf{R}, \mathbf{R}^{\mathrm{MM}}) + V^{\mathrm{MM}}(\mathbf{R}^{\mathrm{MM}}) \\ &= V^{\mathrm{EEQM}}(\mathbf{R}, \mathbf{R}^{\mathrm{MM}}) + V_{\mathrm{non\text{-}ES}}^{\mathrm{QM\text{-}MM}}(\mathbf{R}, \mathbf{R}^{\mathrm{MM}}) \\ &\quad + V^{\mathrm{MM}}(\mathbf{R}^{\mathrm{MM}}) \end{aligned} \tag{1}$$

where $\mathbf{R}$ and $\mathbf{R}^{\mathrm{MM}}$ represent the coordinates of atoms in the QM region and those of atoms in the MM region, respectively. V^{EEQM}, $V_{\mathrm{non\text{-}ES}}^{\mathrm{QM\text{-}MM}}$, and V^{MM} represent the electrostatically embedded QM energy where the electronic wave function is involved, the nonelectrostatic QM-MM energy, and the MM energy.

Because the number of atoms in the MM region is generally much larger than that in the QM region, for efficient calculation of the MMSIC method, first we introduce the electrostatic (ES) potential at atom a in the QM region, Φ_a, from the MM region

$$\Phi_a = \sum_{A=1} \frac{Q_A^{\mathrm{MM}}}{|\mathbf{R}_a - \mathbf{R}_A^{\mathrm{MM}}|} \tag{2}$$

Second, we approximate that V^{EEQM} is expressed by the sum of two terms

$$V^{\mathrm{EEQM}}(\mathbf{R}, \mathbf{\Phi}) \simeq V^{\mathrm{MM}}(\mathbf{R}) + V^{\mathrm{SIC}}(\mathbf{R}, \mathbf{\Phi}) \tag{3}$$

Here, V^{MM} is conventional MM force fields expressed by simple analytical functions and V^{SIC} is determined using the following modified Shepard interpolation so that the sum with V^{MM} reproduces V^{EEQM}

$$V^{\mathrm{SIC}}(\mathbf{R}, \mathbf{\Phi}) = \sum_{k=1}^{N^{\mathrm{SIC}}} W_k(\mathbf{s}(\mathbf{R})) V_k(\mathbf{s}(\mathbf{R}), \mathbf{\Phi}) \tag{4}$$

where N^{SIC} is the number of reference points called the Shepard points. V_k is the energy evaluated by a second-order Taylor expansion around the Shepard point k ($\mathbf{s}_k$, Φ_k) expressed by internal coordinates, $\mathbf{s}$, in the QM region and ES potentials, $\mathbf{\Phi}$. W_k is the normalized weight function of the Shepard point k given by

$$W_k(\mathbf{s}) = \left(\frac{1}{d_k(\mathbf{s})}\right)^4 \Big/ \sum_{k=1}^{N^{\mathrm{SIC}}} \left(\frac{1}{d_k(\mathbf{s})}\right)^4 \tag{5}$$

Here, d_k is the generalized distance expressed by

$$d_k(\mathbf{s}) = \left(\sum_{l=1}^{N^{\mathrm{GD}}} \sin^2(\Delta\phi_l^{(k)}/2)\right)^{1/2} \tag{6}$$

where N^{GD} is the number of torsion angles ϕ_l used in the generalized distance because only the torsion angles ϕ_l are used to determine the weight of the Shepard points.[17]

TDDFT was used for the calculation of V^{EEQM}. The QM region consists of one BChl a pigment and one or two ligand(s) coordinated with the central Mg atom of BChl a. The CAM-B3LYP density functional and the 6-31G(d,p) basis set were used. Note that the range-separated parameter μ = 0.20 was used to reproduce the difference of the first excited Q_y absorption energies of BChl a in solutions.[21] The MMSIC potential energy functions determined in our previous study were used for sites 1 and 3−7.[17] Four Shepard points were added to generate a more accurate potential energy surface for site 2, that is, 11 Shepard points in total, and three Shepard points were used for site 8. The errors of the MMSIC potential energy function for the data of MD simulation were ∼1 kcal/mol for all the sites.

2.2. Calculation of Site Energy. The site energy is the difference between the energies in the ground and excited states. It is known that the absorption energies calculated with TDDFT methods are likely to be overestimated.[21−23] Thus, we estimated the difference between the calculated and experimental excitation energies for the site energies in the FMO protein, by calculating the excitation energy of BChl a in triethylamine solution for which experimental results are available. The absorption energies of BChl a were calculated with the QM/MM method at 600 configurations taken from the MD simulations performed for 6 ns at 300 and 77 K with the charges and structure of BChl a in triethylamine solution determined by QM/MM RWFE-SCF method at 300 K.[21] The average calculated absorption energy is 14 690 cm^{-1} at both 300 and 77 K. The experimental absorption energies are 12 970 and 12 910 cm^{-1} at 295 and 4 K, respectively.[24] In this study, thus, the calculated site energy at each BChl in the FMO protein is shifted by 1720 and 1780 cm^{-1} at 300 and 77 K, respectively, by assuming that the excitation energy at 77 K is close to that at 4 K. The effect of the hydrogen bond between the 3-acetyl and 13^1-keto groups of BChl a on the site energy is corrected as our previous study.[17]

2.3. Calculation of Excitonic Coupling. Excitonic couplings between pigments have been calculated with the transition charges from electrostatic potential (TrESP).[25] In the TrESP method, the excitonic coupling between sites m and n, V_{mn}, is approximated by the interaction between transition charges

$$V_{mn} = \int\int \frac{\rho_m^{\mathrm{Tr}}(\mathbf{r}_m)\rho_n^{\mathrm{Tr}}(\mathbf{r}_n)}{|\mathbf{r}_m - \mathbf{r}_n|} \mathrm{d}\mathbf{r}_m \, \mathrm{d}\mathbf{r}_n \simeq \sum_{a\in m} \sum_{b\in n} \frac{Q_a^{\mathrm{Tr}} Q_b^{\mathrm{Tr}}}{|\mathbf{R}_a - \mathbf{R}_b|} \tag{7}$$

where $\rho_m^{\mathrm{Tr}}(\mathbf{r}_m)$ is the transition density at position $\mathbf{r}_m$ and Q_a^{Tr} is the transition charge of atom a, which is fixed at the value determined at the optimized geometry in the gas phase with a constraint $\sum_a Q_a^{\mathrm{Tr}} = 0$.

As with the MMSIC method, we express $\mathbf{Q}^{\mathrm{Tr}}$ using the modified Shepard interpolation

$$\mathbf{Q}^{\mathrm{Tr}}(\mathbf{R}, \mathbf{\Phi}) = \sum_{k=1}^{N^{\mathrm{SIC}}} W_k(\mathbf{s}(\mathbf{R})) \mathbf{Q}_k^{\mathrm{Tr}}(\mathbf{s}(\mathbf{R}), \mathbf{\Phi}) \tag{8}$$

Table 1. Exciton Hamiltonian at 300 and 77 K (in cm^{-1})[a]

site	1	2	3	4	5	6	7	8
1	12 390 (12 510)	−125 (−127)	6 (6)	−8 (−8)	8 (8)	−25 (−25)	−7 (−7)	32 (33)
2	−125 (−127)	12 590 (12 720)	36 (37)	9 (9)	3 (3)	13 (14)	4 (4)	6 (6)
3	6 (6)	36 (37)	12 200 (12 310)	−59 (−60)	−1 (0)	−11 (−11)	−2 (−3)	1 (1)
4	−8 (−8)	9 (9)	−59 (−60)	12 390 (12 480)	−83 (−82)	−20 (−20)	−69 (−72)	−2 (−2)
5	8 (8)	3 (3)	−1 (0)	−83 (−82)	12 660 (12 730)	79 (84)	−1 (−3)	5 (5)
6	−25 (−25)	13 (14)	−11 (−11)	−20 (−20)	79 (84)	12 450 (12 540)	39 (37)	−10 (−10)
7	−7 (−7)	4 (4)	−2 (−3)	−69 (−72)	−1 (−3)	39 (37)	12 390 (12 520)	−13 (−13)
8	32 (33)	6 (6)	1 (1)	−2 (−2)	5 (5)	−10 (−10)	−13 (−13)	12 660 (12 750)

[a]Values in parenthesis are at 77 K.

Here, N^{SIC} is the number of the Shepard points, W_k is the normalized weight function at the Shepard point k given by eq 5, and $\mathbf{Q}_k^{Tr}$ is the transition charge around the Shepard point k evaluated by the first-order Taylor expansion with respect to the displacements of the internal coordinates in the QM region and the external ES potentials

$$\mathbf{Q}_k^{Tr}(\mathbf{s}, \mathbf{\Phi}) = \mathbf{Q}_k^{Tr0} + \boldsymbol{\kappa}_k^{Tr}\Delta\mathbf{s}_k + \boldsymbol{\chi}_k^{Tr}\Delta\mathbf{\Phi}_k \quad (9)$$

where $\mathbf{Q}_k^{Tr0}$ is the transition charge at the Shepard point k, $\boldsymbol{\kappa}_k^{Tr} \equiv (\partial\mathbf{Q}^{Tr}/\partial\mathbf{s})_{\mathbf{s}_k,\mathbf{\Phi}_k}$ and $\boldsymbol{\chi}_k^{Tr} \equiv (\partial\mathbf{Q}^{Tr}/\partial\mathbf{\Phi})_{\mathbf{s}_k,\mathbf{\Phi}_k}$. $\boldsymbol{\kappa}_k^{Tr}$ and $\boldsymbol{\chi}_k^{Tr}$ express the response functions of $\mathbf{Q}_k^{Tr}$ to the changes of structure and ES potential, which are regarded as charge response kernels (CRKs).[26,27] Notably, the net neutrality of the transition charges in eq 9 is always satisfied because $\sum_a(\boldsymbol{\kappa}_k^{Tr})_{al} = \sum_a(\boldsymbol{\chi}_k^{Tr})_{ab} = 0$ (l and b represent the indexes for the internal coordinate and atom, respectively) due to the constraint $\sum_a Q_a^{Tr} = 0$.

We calculated the excitonic couplings using eqs 7−9, which are called the transition charge response kernel (TrCRK) method hereafter. $\mathbf{Q}_k^{Tr0}$, $\boldsymbol{\kappa}_k^{Tr}$, and $\boldsymbol{\chi}_k^{Tr}$ were evaluated using TDDFT calculations with the CAM-B3LYP (μ = 0.20) functional and the 6-31G(d,p) basis set. $\boldsymbol{\kappa}_k^{Tr}$ and $\boldsymbol{\chi}_k^{Tr}$ were obtained by numerical differentiation of the transition charges. The calculated transition dipole of BChl *a* in the gas phase is 7.6 Debye, whereas the experimental transition dipole is estimated as 6.1 Debye.[28] It is known that the calculated transition dipoles of BChl *a* and Chl *a* are overestimated.[25] Thus, we introduced a scale factor of 0.803 (=6.1/7.6) for $\mathbf{Q}_k^{Tr0}$, as in the previous study.[25] Figure S1 shows the distributions of the transition charges, demonstrating that the largest standard deviation during the MD simulation is ∼0.07. We found that the fluctuation of the transition dipole is properly described by considering the effect of the fluctuations of external ES potential and pigment structure: the mean unsigned error (MUE) between the transition dipoles calculated with the TrCRK and QM/MM calculations, $|\boldsymbol{\mu}^{TrCRK} - \boldsymbol{\mu}^{QM/MM}|$, for the data of MD simulation is 0.22 Debye, whereas the MUE is 0.73 Debye when the TrESP method is used. The obtained exciton Hamiltonians at 300 and 77 K are given in Table 1.

2.4. Computational Details of MD Simulations. We used the *holo* form (eight BChl *a* pigments per monomer) of X-ray crystal structure of the FMO trimer from *Prosthecochloris aestuarii* (PDB code: 3EOJ)[29] for the initial geometry. The FMO trimer was embedded in a rectangular water box of 125 × 125 × 98 $Å^3$ with the periodic boundary condition, in which nine sodium cations are added to neutralize the system with 46364 water molecules. The proteins and water molecules were treated by the Amber ff99SB-ILDN[30] and TIP3P force field.[31]

First, we performed MD simulations for 10 ns with MM force fields for all the molecules to equilibrate the total system, as in our previous study.[17] Then, the potential energy functions of all the 24 BChl *a* pigments and their ligands were switched from the MM force fields to the MMSIC potential energy functions. We performed equilibrium MD simulations with the MMSIC potential energy functions for 1 ns at 300 K in the ground state, followed by 1 ns MD simulation for data production. Three independent MD simulations were carried out to increase the statistics. For the MD simulations at 77 K, 300 configurations were taken every 10 ps from the trajectory at 300 K because of the difficulty of sampling various configurations in simulations at low temperature. After the geometry optimizations were carried out, we performed equilibrium MD simulations for 10 ps at 77 K, followed by 10 ps MD simulation for data production. Therefore, the total simulation length corresponds to 3 ns, that is, 300 × 10 ps. As the FMO complex consists of trimer subunits, 9 ns of MD trajectory data for each site were used for analyses at both 300 and 77 K. All the electronic structure calculations and MD simulations were performed using our modified version of GAMESS,[32] AMBERPLUS,[33] MCSI,[34] and AMBER 15[35] program packages.

3. RESULTS AND DISCUSSION

3.1. Site Energies and Distributions. Figures 1c and S2a show the calculated site energies at 300 and 77 K as well as the fitted results based on experimental data at cryogenic temperature.[36−41] The site energies are shifted by 1720 and 1780 cm^{-1} at 300 and 77 K, respectively, as mentioned above. Note here that the energy shifts are determined for BChl *a* in triethylamine solution, not for that in the FMO protein. The calculated site energies of all the sites at both the temperatures are, however, in good agreement with those determined from the experimental results. It has been shown that a proper description of intra- and intermolecular interactions is important to reproduce the site energies fitted to the experimental spectra by using simulations.[16,22,42,43] We have also shown that the electronic properties of BChl *a* show a strong functional dependence in DFT calculations, and thus, the use of an appropriate functional is essential for the calculation of site energies.[21] The present result shows that BChl 3 has the lowest site energy because of stable intermolecular interactions, especially the large stabilization (∼190 cm^{-1}) by the hydrogen bond between Tyr15 and the acetyl group of site 3, which is consistent with the mutation experiment of Tyr to Phe, which results in an increase of the site energy by ∼170 cm^{-1}.[44]

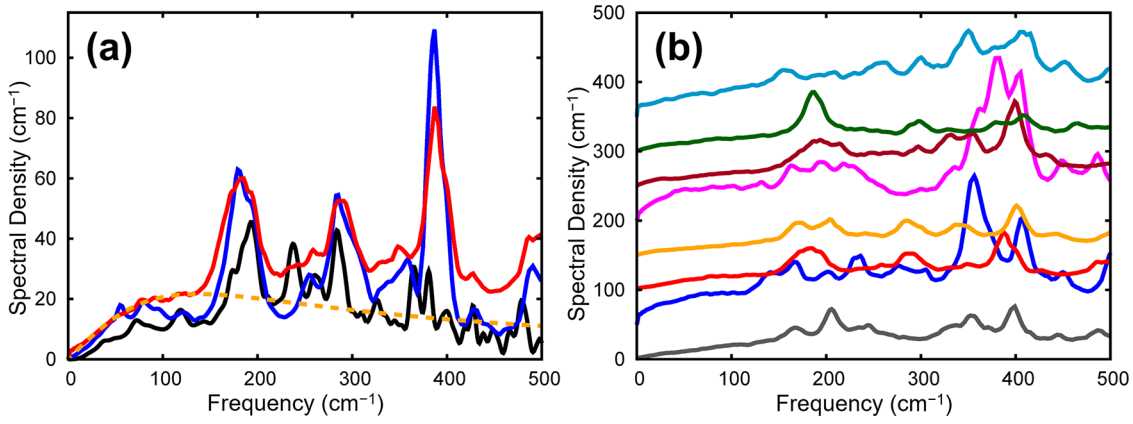

Figure 2. (a) Comparison of the experimental spectral density of the lowest energy level at 4 K[47] (black) with the calculated spectral densities of site 3 at 300 K (red) and 77 K (blue). Dashed orange curve is the Drude–Lorentz spectral density at 300 K. (b) Calculated spectral densities of eight sites at 300 K. Spectral densities are arranged in order from site 1 to site 8 with an offset of 50 cm^{-1} for clarity. The spectral densities at sites 1, 2, 3, 4, 5, 6, 7, and 8 are shown by gray, blue, red, orange, magenta, brown, green, and sky-blue lines, respectively.

Table 2. Parameters of the Drude–Lorentz Spectral Density and Kubo's Stochastic Theory for Line Shape[a]

site	1	2	3	4	5	6	7	8
λ_n	70 (44)	144 (121)	68 (50)	51 (29)	151 (95)	65 (43)	67 (37)	131 (86)
γ_n	171 (142)	87 (96)	137 (94)	148 (117)	73 (109)	145 (184)	162 (95)	120 (97)
$\Delta_n T_n$	0.51 (0.48)	1.43 (1.19)	0.62 (0.78)	0.50 (0.48)	1.74 (0.93)	0.36 (0.37)	0.52 (0.66)	0.99 (0.99)

[a] λ_n and γ_n are in cm^{-1}. Values in parenthesis are at 77 K.

The present result shows that sites 2, 5, and 8 have large site energies. The origins of their large site energies differ; they result from the polar environment around site 2, the steric hindrance of the twisted acetyl group of site 5, and the less stable intermolecular interaction at site 8 because the site exists between two subunits. In addition, unlike Mg atoms in the other sites with five coordinates, the Mg atom of site 8 has six coordinates: the fifth and sixth ligands of site 8 are the main chain CO group of Try123 and the side chain OH group of Ser168, respectively.

Figures 1d and S3 show the distributions of site energies at 300 and 77 K, respectively. The site energies of sites 1, 3, 4, 6, and 7 show Gaussian distributions, whereas those of sites 2, 5, and 8 show broad non-Gaussian distributions.[16,17,45,46] The non-Gaussian distributions of sites 2, 5, and 8 are attributed to the inhomogeneous fluctuations of site energy under the polar environment, the steric hindrance, and the inhomogeneous intra- and intermolecular interactions, respectively.

3.2. Fluctuation of Site Energies and Spectral Densities. We examine the dynamic fluctuation of site energies using the time correlation function (TCF) of the site energies at sites m and n

$$C_{mn}(t) = \langle \delta E_m(0)\delta E_n(t)\rangle \tag{10}$$

where δE_m is the deviation of site energy from the average site energy of site m, that is, $\delta E_m(t) = E_m(t) - \langle E_m\rangle$. We find that the correlations between different sites are much smaller than that of each site; the smallest site energy fluctuation in the same site, $C_{44}(0)$, is more than 20 times larger than the largest site energy fluctuation between different sites, $C_{56}(0)$. Thus, we neglect the site energy fluctuations between different sites in this study.

We examine the site energy fluctuation in terms of the spectral density defined as the following equation

$$J_n(\omega) = \frac{\beta\omega}{\pi}\int_0^\infty C_{nn}(t)\cos(\omega t)\mathrm{d}t \tag{11}$$

where β is the inverse temperature. Here, we assume the so-called harmonic quantum correction for detailed balance. Figure 2a shows a comparison between the experimental spectral density of site with the lowest site energy[47] and the calculated spectral densities of site 3 at 300 and 77 K. The overall shape and amplitude of the calculated spectral density are in good agreement with the experimental result. The spectral densities of eight sites at 300 and 77 K are shown in Figures 2b and S4. Note here that the spectral densities show strong site and temperature dependences. The spectral densities of sites 2, 5, and 8 are approximately twice as large as those of the other sites because of slow and large fluctuations of intra- and intermolecular interactions. As shown in previous studies, the peaks at ~200 and ~400 cm^{-1} are attributed to the in-plane bacteriochlorin ring motions.[17,24]

The spectral density has frequently been approximated using the Drude–Lorentz density

$$J_n(\omega) = \frac{1}{\pi}\frac{2\lambda_n\gamma_n\omega}{\omega^2 + \gamma_n^2} \tag{12}$$

Here, λ_n and γ_n represent the magnitude of fluctuation and the modulation rate of site energy fluctuation of site n, respectively, and are expressed as $\lambda_n = \beta\langle\delta E_n^2\rangle/2 \equiv \beta\Delta_n^2/2$ and $\gamma_n = 1/T_n$. λ_n and T_n are the reorganization energy and the characteristic time scale of energy fluctuation at site n induced by the environment, respectively, that is, intra- and intermolecular motions of the FMO protein and solvent molecules. By assuming a high temperature ($\beta\hbar\gamma_n < 1$) for the Drude–Lorentz model, the real and imaginary parts of the site energy fluctuation TCF $C(t)$ become exponential functions. We indeed find that both the parts of $C(t)$ are well approximated

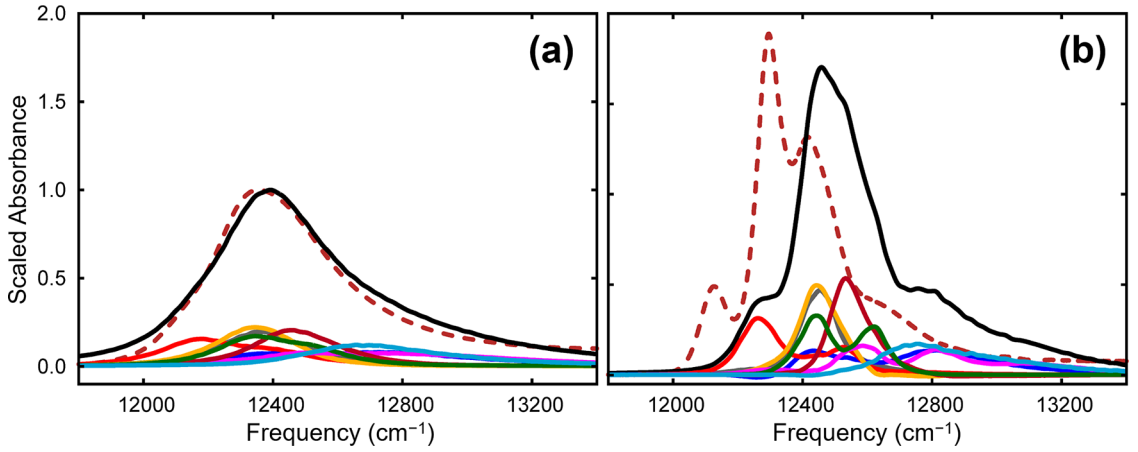

Figure 3. Comparison of calculated absorption spectra at (a) 300 and (b) 77 K with the experimental result[29] (dashed brown line). In (a,b), the absorption spectra of sites 1, 2, 3, 4, 5, 6, 7, and 8 are shown by gray, blue, red, orange, magenta, brown, green, and sky-blue lines, respectively.

by exponential functions for all the sites at 300 K, though the modulation at site 6 is large at 77 K and thus a small negative region exists in its response function.[48]

We characterize the fluctuation at an individual site via Kubo's stochastic theory for line shape.[49] In Kubo's stochastic theory, a fluctuation with $\Delta_n T_n < 1$ is categorized as the fast modulation regime, whereas that with $\Delta_n T_n > 1$ is the slow modulation regime. The parameters, λ_n, γ_n, and $\Delta_n T_n$, of each site are presented in Table 2. The present result reveals that the fluctuations at sites 1, 3, 4, 6, and 7 are in the fast modulation regime, that is, $\Delta_n T_n \leq 0.6$. It is of interest that site 3 having the lowest site energy exhibits the largest $\Delta_n T_n$ of these five sites. The moderately large fluctuation at site 3 can contribute to the stabilization of the lowest excitonic state and to the facilitation of the EET from site 3 to the RC. In contrast to sites 1, 3, 4, 6, and 7, sites 2, 5, and 8 with large site energies have fluctuations in the intermediate to slow modulation regimes, that is, $\Delta_n T_n \geq 1$.

3.3. Absorption Spectrum. Absorption spectra are calculated with the numerical integration of the Schrödinger equation[50]

$$I(\omega) = \omega \mathrm{Re} \int_0^\infty \mathrm{d}t\ \mathrm{e}^{\mathrm{i}\omega t}\ \mathrm{Im} \left\langle \sum_{m,n}^{N_{\mathrm{site}}} \mathbf{d}_m(t) \mathbf{U}_{mn}(t) \mathbf{d}_n(0) \right\rangle \tag{13}$$

Here, $\mathbf{d}_m(t)$ are $\mathbf{U}(t)$ are the transition dipole moment vector of site m at t and the time evolution matrix from $t = 0$ to t, respectively. The transition dipole moments were calculated from the transition charges used for the calculation of exciton couplings.

The calculated absorption spectra at 300 and 77 K as well as the experimental spectra[29] are shown in Figure 3. The amplitudes of experimental and calculated spectra are scaled with those at 300 K. The calculated spectrum at 77 K is blue shifted by ~160 cm^{-1} and the peak structure at 12 500 cm^{-1} is slightly weakened, compared with the experimental result. These differences may be due to the simulated conformations not being fully relaxed at 77 K. However, the line shape and relative intensity of calculated absorption spectra are in good agreement with the experimental spectra.

To clarify the contributions of individual sites to the total absorption spectra, we calculate the spectra of individual sites. As can be seen in the spectra at 300 and 77 K (Figure 3a,b), the lowest energy peak is attributed to the absorption of site 3 and the higher energy peak mainly arises from the absorptions of sites 2, 5, and 8. On the other hand, the peak at ~12 450 cm^{-1} is attributed to the absorptions of sites 1, 4, 6, and 7; the shoulder at ~12 800 cm^{-1} is mainly attributed to sites 4, 6, and 7; and the low-frequency tails of sites 5 and 8.

In order to examine the effect of fluctuations of individual sites on the absorption spectrum, we compare the individual absorption spectrum with the distribution of the site energy, which corresponds to the limit of an inhomogeneously broadened spectrum for each site (Figure S4). We analyze the ratio between the widths of the absorption spectrum and distribution of site energy of each site. The extent of inhomogeneity at each site is qualitatively given by the ratio between the individual absorption spectrum and site energy distribution. We find that the extent of inhomogeneity at each site evaluated from the ratio is fully consistent with the modulation of spectral density determined by Kubo's stochastic theory (Table S2), that is, the modulations of transition frequencies of sites 1, 3, 4, 6, and 7 are characterized as the fast modulation, that is, the motional narrowing regime, whereas those of sites 2, 5, and 8 are rather intermediate between the fast and slow modulation regimes.

Recently, Cao and co-workers have developed the full second-order cumulant expansion (FCE) method to investigate absorption and emission spectra and Förster resonance energy-transfer rate.[51] It has been shown that the absorption spectra calculated from the method are almost identical to the exact spectra even when the system−bath coupling is far from the perturbative regime. It will be of interest to examine the temperature-dependent shift of the spectral maxima by the FCE method.

3.4. EET Dynamics. Next, we examine the EET in the FMO protein. The time evolution of the reduced density matrix is solved by the hierarchical equations of motion using the conventional Frenkel exciton Hamiltonian (Table 1) and the site-dependent Drude−Lorentz spectral densities for the influence of bath on each site (Table 2).[48,52] As shown previously, when site 1 or 6 is initially excited, the relaxation to site 3 takes place from site 1 to site 2 (pathway 1) or from site 6 to sites 5, 7, and 4 (pathway 2) with coherent oscillations (Figure S5).[53−59] When site 8 is initially excited, the population mainly relaxes via pathway 1 and very weak oscillatory structures are found only in the population of sites 1

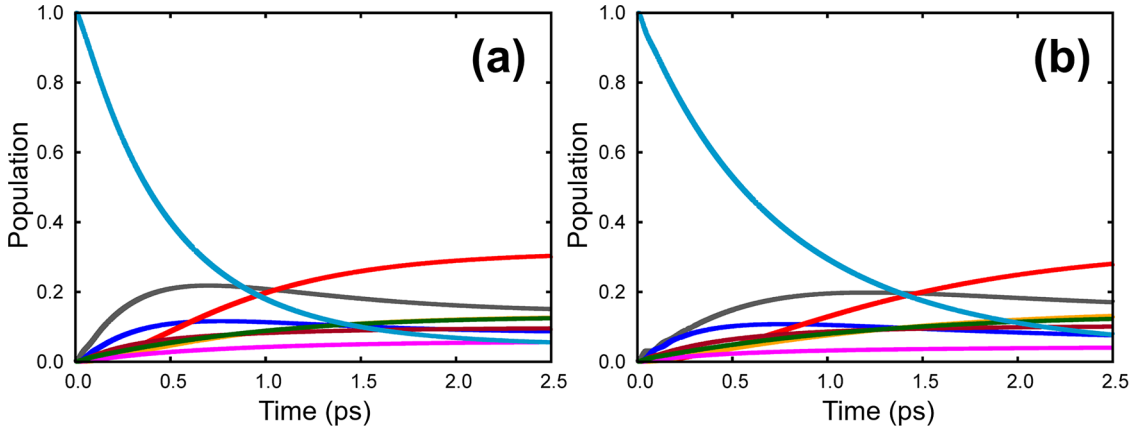

Figure 4. Population dynamics after the initial excitation of site 8 at 300 K calculated with (a) site-dependent spectral densities determined in this study and with (b) single spectral density determined by Read et al. used for all the eight sites. In (a,b), the populations of sites 1, 2, 3, 4, 5, 6, 7, and 8 are shown by gray, blue, red, orange, magenta, brown, green, and sky-blue lines, respectively.

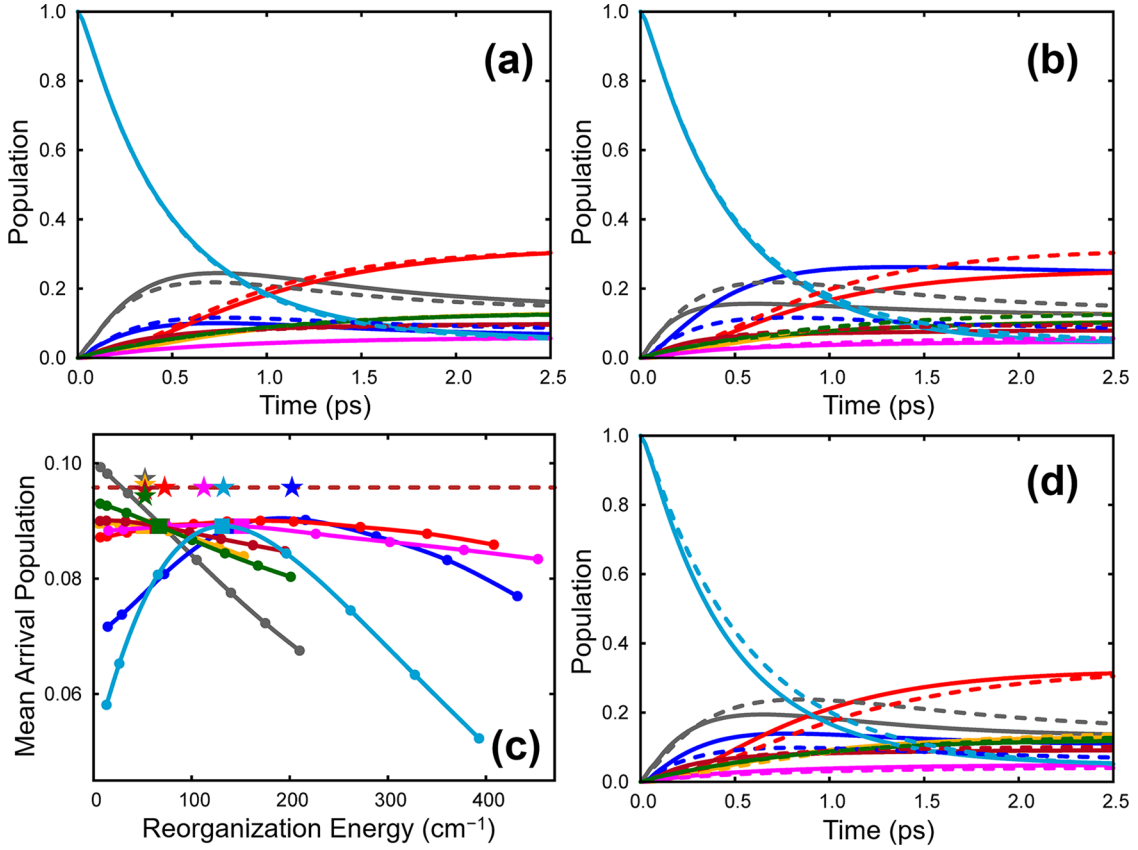

Figure 5. Population dynamics after the initial excitation of site 8 at 300 K calculated with the reorganization energy of (a) 72 and (b) 432 cm^{-1} at site 2. In (a,b), the dynamics calculated with the original reorganization energy (144 cm^{-1}) are shown by the dashed line. (c) $\bar{\alpha}(t = 1\ \text{ps})$ with respect to the reorganization energy of each site at 300 K. Squares correspond to the original reorganization energy at each site. The dashed line is $\bar{\alpha}(t = 1\ \text{ps})$ (=0.096) obtained with the optimized set of reorganization energies and the colored stars are the reorganization energy of each site in the optimized set at 300 K. (d) Population dynamics calculated with the fully optimized reorganization energies (solid line) and with the single reorganization energy fixed at the average of the optimized set of the eight values (dashed line). Stars are the optimized reorganization energy at each site. In (a–d), the populations, $\bar{\alpha}(t = 1\ \text{ps})$, and stars of sites 1, 2, 3, 4, 5, 6, 7, and 8 are shown by gray, blue, red, orange, magenta, brown, green, and sky-blue lines, respectively.

and 2 at 77 K within ~200 fs (Figure S5b).[41,57,58,60] Because it is conceivable from recent experiments that site 8 is the acceptor from the chlorosome,[5] we mainly discuss the relaxation dynamics from site 8 hereafter.

The present result shows that the FMO protein consists of the sites with heterogeneous fluctuations extending from the fast to slow modulation. To elucidate the effect of site-dependent fluctuation on the dynamics, we compare the dynamics calculated with the present site-dependent spectral densities with those calculated with the single spectral density determined by Read et al. for all the sites.[40] The spectral density determined by Read et al. (λ = 35 cm^{-1} and γ = 106

Table 3. Optimized Set of Reorganization Energies at 300 and 77 K[a]

site	1	2	3	4	5	6	7	8
λ_n	50 (30)	200 (290)	70 (50)	50 (70)	110 (220)	50 (30)	50 (30)	130 (170)

[a] λ_n is in cm^{-1}. Values in parenthesis are at 77 K. λ_3 is fixed to be 70 and 50 cm^{-1} at 300 and 77 K, respectively. Minimum values of 50 and 30 cm^{-1} are assumed at 300 and 77 K, respectively.

cm^{-1}) is characterized as a fast modulation ($\Delta T \approx 0.6$), similar to the modulations at sites 1, 4, 6, and 7. Figure 4a,b shows the population dynamics calculated with the site-dependent individual spectral densities and the single spectral density for all the sites. To quantify the efficiency of EET to site 3, we introduce the mean arrival population at site 3, measuring the average increase in the population at site 3 during time t

$$\bar{\alpha}(t) = \frac{1}{t}\int_0^t (\rho_{33}(\tau) - \rho_{33}(0))\mathrm{d}\tau \tag{14}$$

Here, $\rho_{33}(0) = 0$ in the relaxation from site 8. We calculate the mean arrival population at 1 ps because the population of site 3 has almost the largest value among eight sites at ~1 ps. It should also be noted that the excitation-transfer rate to the RC has been assumed to be ~1 ps in recent studies.[61−63] We find that $\bar{\alpha}(t = 1\ \mathrm{ps})$ is 0.089 and 0.051 for the system with the site-dependent individual and single spectral densities, respectively. Furthermore, we emphasize that similarly inefficient EET with the single spectral density is found in the relaxations from site 1 or site 6 at 300 and 77 K. These results suggest that the EET is accelerated by the presence of spatial heterogeneous fluctuations in the system.

3.5. Efficient EET Achieved by Site-Dependent Fluctuations. We here consider how the EET dynamics depend on the spectral density of an individual site. First, we find that the EET dynamics depend more strongly on the reorganization energy, λ, than the modulation rate, γ, by examining the λ- and γ-dependence of $\bar{\alpha}(t = 1\ \mathrm{ps})$. Thus, we explore the detailed dynamics with respect to the λ-dependence at the various sites.

Figure 5a,b shows the population dynamics calculated with a half (72 cm^{-1}) and triple (432 cm^{-1}) of the original reorganization energy at site 2. For a small reorganization energy at site 2, λ_2, the dynamics from site 1 to 2 and site 2 to 3 are slow because of large deviations from the resonance conditions (Figure 5a) but become fast with increasing λ_2. On the other hand, for a very large λ_2, the relaxation from sites 2−3 is decelerated because of the trapping of the exciton at site 2, that is, the increase (decrease) in the equilibrium population at site 2 (site 3) (Figure 5b). Thus, the relaxation rate is decelerated and the amount of energy relaxed to site 3 is decreased. Thus, as can be seen in Figure 5c, $\bar{\alpha}(t = 1\ \mathrm{ps})$ shows a bell-shaped dependence with the maximum at $\lambda_2 \approx 215$ cm^{-1}. $\bar{\alpha}(t = 1\ \mathrm{ps})$ at site 8 also shows a bell-shaped dependence because of the same mechanism seen in $\bar{\alpha}(t = 1\ \mathrm{ps})$ at site 2 (Figure S6a,b). We also find bell-shaped $\bar{\alpha}(t = 1\ \mathrm{ps})$ with respect to λ_2 and λ_8 at 77 K.

Ishizaki and Fleming have examined the relationship between the energy-transfer rate and the reorganization energy λ for the two-state model and found the maximum energy-transfer rate at $\lambda \approx J$, that is, the electronic coupling between the two states.[64,65] In addition, environmental effects on the dynamics in the model FMO protein expressed by a single spectral density for all the sites have been investigated and the presence of optimal parameters has been shown.[61−63,66,67] The presence of the optimized reorganization energy at site 2 or 8 is consistent with the results, though the relationship between the optimized λ and J is not simple in the multiple-site system.

In contrast, at site 1, the reorganization energy dependence of $\bar{\alpha}(t = 1\ \mathrm{ps})$ is different from those found at sites 2 and 8. With the increase of the reorganization energy at site 1, the EET is monotonically delayed by the trapping of the exciton at site 1, that is, the increase in the equilibrium population at site 1 and thus the EET to site 3 becomes inefficient (Figure S6c,d). A similar reorganization energy dependence is found at sites 4, 6, and 7, whose site energies are low. In addition, at sites 3 and 5, the efficiency, that is, $\bar{\alpha}(t = 1\ \mathrm{ps})$, is almost independent of the reorganization energy at 300 K.

The requirements for an optimal energy-transfer rate in a dimer system or systems with a single reorganization energy are well characterized and understood. However, in a multisite system with several potential pathways for energy flow, the situation is much more complex, as shown above. Optimizing a given pairwise rate may adversely affect onward transfer from the acceptor site, for example. Here, we explored the role of the individual site fluctuations via the reorganization energies of the eight sites on the overall energy flow from site 8 to site 3.

We determined an optimized set of reorganization energies at 300 or 77 K to maximize $\bar{\alpha}(t = 1\ \mathrm{ps})$ using the reorganization energies obtained from the MD simulations as initial values. We assumed a minimum value of 50 cm^{-1} for sites 1, 4, 6, and 7 to avoid unphysically small reorganization energies, and fixed λ at the original value of 70 cm^{-1} for site 3 because the difference between site 3 and RC is approximately 120 cm^{-1}[68,69] and a too large reorganization energy at site 3 may inhibit efficient EET to the RC (Table 3). The time evolution of the resultant populations calculated with the optimized set (solid line) as well as those with the single reorganization energy, fixed at the average (88.8 cm^{-1}) of the optimized set (dashed line), are shown in Figure 5d. The result shows that the fluctuations at individual sites produce efficient EET by enhancing the resonant condition between neighboring sites with large site energy differences and avoiding trapping of the exciton on the relaxation pathway(s) ($\bar{\alpha}(t = 1\ \mathrm{ps}) = 0.096$, whereas a value of 0.075 is obtained with the averaged single reorganization energy for all the sites). We further find that the difference between $\bar{\alpha}(t = 1\ \mathrm{ps})$ calculated with the optimized reorganization energies (0.096) and the original spectral densities (0.089) is small at 300 K, whereas the corresponding difference is large at 77 K, that is, $\bar{\alpha}(t = 1\ \mathrm{ps})$ are 0.217 and 0.102, respectively (Figure S7). The present study thus demonstrates that the site-dependent reorganization energies in the FMO protein that we obtained are approximately optimized at room temperature.

4. CONCLUSIONS

In the present study, we developed the MD simulation method that can describe the site energies of pigments and the excitonic couplings between pigments accurately and efficiently, by considering the fluctuations of external electrostatic potential and BChl structure. By applying the method to the FMO protein, we successfully obtained the individual site

energies and spectral densities of BChls, which are in good agreement with the existing experimental results. Furthermore, it was found that the present method can reproduce the experimental absorption spectra of the FMO protein at 300 and 77 K.

By examining the spectral densities at individual sites, we found remarkable site-dependent fluctuations in the FMO protein due to the heterogeneity of their local environment. Based on Kubo's stochastic theory for line shape, we found that the fluctuations of sites 1, 3, 4, 6, and 7 are characterized as the fast modulation, whereas sites 2, 5, and 8 have fluctuations in the intermediate to slow modulation regimes.

We also found that the efficient EET dynamics are achieved at 300 K with the approximately optimized site-dependent reorganization energies. Similar results showing that efficient EET dynamics are achieved by the environment at room temperature have been reported for model systems with a single spectral density for all the sites. However, we revealed that efficient EET is achieved by the differing roles of site-dependent fluctuations from fast to slow modulation: large fluctuations at sites with large site energies result in the enhancement of resonance between their neighboring sites, while small fluctuations at sites with small site energies facilitate avoidance of exciton trapping. In addition to these roles at the sites internal to the FMO protein, we expect that fluctuations at site 8 can be effective in the EET from chlorosome and that those at site 3 can facilitate EET to the RC.

In this study, we examined the relaxation dynamics using the Drude–Lorentz model, by neglecting the underdamped intra- and intermolecular vibrations. The effects of underdamped vibrations on coherence and energy transfer have been intensively studied.[70−77] A detailed discussion of vibrational effects on the dynamics will be given elsewhere.

Overall in the FMO protein, excitation energy is transferred on a rugged site energy landscape with highly heterogeneous local fluctuations. It is not easy to reveal how the present energy-transfer pathway has been acquired in the course of evolution. Detailed information on the fluctuations in the FMO protein does, however, provide clues as to the optimization of efficient EET in natural photosynthetic systems and suggests strategies for the development of artificial photosynthetic systems.

■ ASSOCIATED CONTENT

Supporting Information

The Supporting Information is available free of charge on the ACS Publications website at DOI: 10.1021/acs.jpcb.9b07456.

Extent of inhomogeneities evaluated from the absorption spectrum and site energy distribution at each site; distributions of transition charges, calculated site energies, excitonic levels, distribution of site energies, and spectral densities of eight sites at 77 K; comparison of the absorption spectrum with the distribution of site energy of each site at 300 and 77 K; population dynamics after the initial excitation of sites 8, 1, and 6 at 300 and 77 K; those after the initial excitation of site 8 with several reorganization energies at sites 8 and 1 at 300 K; and $\bar{\alpha}(t = 1\ \mathrm{ps})$ with respect to the reorganization energy of each site at 77 K (PDF)

■ AUTHOR INFORMATION

Corresponding Author

*E-mail: shinji@ims.ac.jp.

ORCID

Shinji Saito: 0000-0003-4982-4820
Masahiro Higashi: 0000-0001-9829-389X
Graham R. Fleming: 0000-0003-0847-1838

Notes

The authors declare no competing financial interest.

■ ACKNOWLEDGMENTS

The authors are grateful to Professor Robert E. Blankenship for providing us with his experimental data. S.S. was supported by JSPS KAKENHI grant no. JP16H02254 and the Indo (DST)-Japan (JSPS) bilateral collaboration program and M.H. was supported by JSPS KAKENHI grant nos. JP16KT0165, JP17K05757, JP18H04657, and JST PRESTO grant no. JPMJPR18GA. G.R.F. was supported by the US Department of Energy, Basic Energy Sciences, Chemical Sciences, Geosciences, and Biosciences Division. The calculations were carried out by using the supercomputers at Research Center for Computational Science in Okazaki.

■ REFERENCES

(1) van Amerongen, H.; Valkunas, L.; van Grondelle, R. *Photosynthetic Excitons*; World Scientific: Singapore, 2000.

(2) Blankenship, R. E. *Molecular Mechanisms of Photosynthesis*; Blackwell Science: Oxford, 2002.

(3) Fenna, R. E.; Matthews, B. W. Chlorophyll Arrangement in a Bacteriochlorophyll Protein from *Chlorobium limicola*. *Nature* **1975**, *258*, 573−577.

(4) Li, Y.-F.; Zhou, W.; Blankenship, R. E.; Allen, J. P. Crystal Structure of the Bacteriochlorophyll *a* Protein from *Chlorobium tepidum*. *J. Mol. Biol.* **1997**, *271*, 456−471.

(5) Wen, J.; Zhang, H.; Gross, M. L.; Blankenship, R. E. Native Electrospray Mass Spectrometry Reveals the Nature and Stoichiometry of Pigments in the FMO Photosynthetic Antenna Protein. *Biochemistry* **2011**, *50*, 3502−3511.

(6) Savikhin, S.; Buck, D. R.; Struve, W. S. Oscillating Anisotropies in a Bacteriochlorophyll Protein: Evidence for Quantum Beating between Exciton Levels. *Chem. Phys.* **1997**, *223*, 303−312.

(7) Engel, G. S.; Calhoun, T. R.; Read, E. L.; Ahn, T.-K.; Mančal, T.; Cheng, Y.-C.; Blankenship, R. E.; Fleming, G. R. Evidence for Wavelike Energy Transfer through Quantum Coherence in Photosynthetic Systems. *Nature* **2007**, *446*, 782−786.

(8) Panitchayangkoon, G.; Hayes, D.; Fransted, K. A.; Caram, J. R.; Harel, E.; Wen, J.; Blankenship, R. E.; Engel, G. S. Long-lived quantum coherence in photosynthetic complexes at physiological temperature. *Proc. Natl. Acad. Sci. U.S.A.* **2010**, *107*, 12766−12770.

(9) Wen, J.; Zhang, H.; Gross, M. L.; Blankenship, R. E. Membrane Orientation of the FMO Antenna Protein from *Chlorobaculum tepidum* as Determined by Mass Spectrometry-Based Footprinting. *Proc. Natl. Acad. Sci. U.S.A.* **2009**, *106*, 6134−6139.

(10) Fleming, G. R.; Schlau-Cohen, G. S.; Amarnath, K.; Zaks, J. Design principles of photosynthetic light-harvesting. *Faraday Discuss.* **2012**, *155*, 27−41.

(11) Mirkovic, T.; Ostroumov, E. E.; Anna, J. M.; van Grondelle, R.; Govindjee; Scholes, G. D. Light Absorption and Energy Transfer in the Antenna Complexes of Photosynthetic Organisms. *Chem. Rev.* **2017**, *117*, 249−293.

(12) Olbrich, C.; Strümpfer, J.; Schulten, K.; Kleinekathöfer, U. Theory and Simulation of the Environmental Effects on FMO Electronic Transitions. *J. Phys. Chem. Lett.* **2011**, *2*, 1771−1776.

(13) Renger, T.; Klinger, A.; Steinecker, F.; Schmidt am Busch, M.; Numata, J.; Müh, F. Normal mode analysis of the spectral density of

the Fenna-Matthews-Olson light-harvesting protein: how the protein dissipates the excess energy of excitons. *J. Phys. Chem. B* **2012**, *116*, 14565−14580.
(14) Rivera, E.; Montemayor, D.; Masia, M.; Coker, D. F. Influence of Site-Dependent Pigment-Protein Interactions on Excitation Energy Transfer in Photosynthetic Light Harvesting. *J. Phys. Chem. B* **2013**, *117*, 5510−5521.
(15) Jia, X.; Mei, Y.; Zhang, J. Z. H.; Mo, Y. Hybrid QM/MM Study of FMO Complex with Polarized Protein-Specific Charge. *Sci. Rep.* **2015**, *5*, 17096.
(16) Wang, X.; Ritschel, G.; Wüster, S.; Eisfeld, A. Open Quantum System Parameters for Light Harvesting Complexes from Molecular Dynamics. *Phys. Chem. Chem. Phys.* **2015**, *17*, 25629−25641.
(17) Higashi, M.; Saito, S. Quantitative Evaluation of Site Energies and Their Fluctuations of Pigments in the Fenna-Matthews-Olson Complex with an Efficient Method for Generating a Potential Energy Surface. *J. Chem. Theory Comput.* **2016**, *12*, 4128−4137.
(18) Lee, M. K.; Coker, D. F. Modeling Electronic-Nuclear Interactions for Excitation Energy Transfer Processes in Light-Harvesting Complexes. *J. Phys. Chem. Lett.* **2016**, *7*, 3171−3178.
(19) Kim, C. W.; Rhee, Y. M. Constructing an Interpolated Potential Energy Surface of a Large Molecule: A Case Study with Bacteriochlorophyll a Model in the Fenna-Matthews-Olson Complex. *J. Chem. Theory Comput.* **2016**, *12*, 5235−5246.
(20) Kim, C. W.; Choi, B.; Rhee, Y. M. Excited State Energy Fluctuations in the Fenna-Matthews-Olson Complex from Molecular Dynamics Simulations with Interpolated Chromophore Potentials. *Phys. Chem. Chem. Phys.* **2018**, *20*, 3310−3319.
(21) Higashi, M.; Kosugi, T.; Hayashi, S.; Saito, S. Theoretical Study on Excited States of Bacteriochlorophyll *a* in Solutions with Density Functional Assessment. *J. Phys. Chem. B* **2014**, *118*, 10906−10918.
(22) Shim, S.; Rebentrost, P.; Valleau, S.; Aspuru-Guzik, A. Atomistic Study of the Long-Lived Quantum Coherences in the Fenna-Matthews-Olson Complex. *Biophys. J.* **2012**, *102*, 649−660.
(23) König, C.; Neugebauer, J. Protein Effects on the Optical Spectrum of the Fenna-Matthews-Olson Complex from Fully Quantum Chemical Calculations. *J. Chem. Theory Comput.* **2013**, *9*, 1808−1820.
(24) Rätsep, M.; Cai, Z.-L.; Reimers, J. R.; Freiberg, A. Demonstration and Interpretation of Significant Asymmetry in the Low-Resolution and High-Resolution Q_y Fluorescence and Absorption Spectra of Bacteriochlorophyll *a*. *J. Chem. Phys.* **2011**, *134*, 024506.
(25) Madjet, M. E.; Abdurahman, A.; Renger, T. Intermolecular Coulomb Couplings from Ab Initio Electrostatic Potentials: Application to Optical Transitions of Strongly Coupled Pigments in Photosynthetic Antennae and Reaction Centers. *J. Phys. Chem. B* **2006**, *110*, 17268−17281.
(26) Morita, A.; Kato, S. Ab Initio Molecular Orbital Theory on Intramolecular Charge Polarization: Effect of Hydrogen Abstraction on the Charge Sensitivity of Aromatic and Nonaromatic Species. *J. Am. Chem. Soc.* **1997**, *119*, 4021−4032.
(27) Lu, Z.; Yang, W. Reaction Path Potential for Complex Systems Derived from Combined Ab Initio Quantum Mechanical and Molecular Mechanical Calculations. *J. Chem. Phys.* **2004**, *121*, 89−100.
(28) Knox, R. S.; Spring, B. Q. Dipole Strengths in the Chlorophylls. *Photochem. Photobiol.* **2003**, *77*, 497−501.
(29) Tronrud, D. E.; Wen, J.; Gay, L.; Blankenship, R. E. The Structural Basis for the Difference in Absorbance Spectra for the FMO Antenna Protein from Various Green Sulfur Bacteria. *Photosynth. Res.* **2009**, *100*, 79−87.
(30) Lindorff-Larsen, K.; Piana, S.; Palmo, K.; Maragakis, P.; Klepeis, J. L.; Dror, R. O.; Shaw, D. E. Improved side-chain torsion potentials for the Amber ff99SB protein force field. *Proteins* **2010**, *78*, 1950−1958.
(31) Jorgensen, W. L.; Chandrasekhar, J.; Madura, J. D.; Impey, R. W.; Klein, M. L. Comparison of simple potential functions for simulating liquid water. *J. Chem. Phys.* **1983**, *79*, 926−935.
(32) Schmidt, M. W.; Baldridge, K. K.; Boatz, J. A.; Elbert, S. T.; Gordon, M. S.; Jensen, J. H.; Koseki, S.; Matsunaga, N.; Nguyen, K. A.; Su, S.; Windus, T. L.; Dupuis, M.; Montgomery, J. A. General Atomic and Molecular Electronic Structure System. *J. Comput. Chem.* **1993**, *14*, 1347−1363.
(33) Higashi, M.; Truhlar, D. G. *AMBERPLUS, 2010*; University of Minnesota: Minneapolis, MN, 2010.
(34) Tishchenko, O.; Higashi, M.; Albu, T. V.; Corchado, J. C.; Kim, Y.; Villà, J.; Xing, J.; Lin, H.; Truhlar, D. G. *MCSI*; University of Minnesota: Minneapolis, MN, 2010.
(35) Case, D. A.; Berryman, J. T.; Betz, R. M.; Cerutti, D. S.; Cheatham, T. E., III; Darden, T. A.; Duke, R. E.; Giese, T. J.; Gohlke, H.; Goetz, A. W.; Homeyer, N.; Izadi, S.; Janowski, P.; Kaus, J.; Kovalenko, A.; Lee, T. S.; LeGrand, S.; Li, P.; Luchko, T.; Luo, R.; Madej, B.; Merz, K. M.; Monard, G.; Needham, P.; Nguyen, H.; Nguyen, H. T.; Omelyan, I.; Onufriev, A.; Roe, D. R.; Roitberg, A.; Salomon-Ferrer, R.; Simmerling, C. L.; Smith, W.; Swails, J.; Walker, R. C.; Wang, J.; Wolf, R. M.; Wu, X.; Kollman, P. A. *AMBER 2015*; University of California: San Francisco, CA, 2015.
(36) Iseri, E. I.; Gülen, D. Electronic Excited States and Excitation Transfer Kinetics in the Fenna-Matthews-Olson Protein of the Photosynthetic Bacterium *Prosthecochloris aestuarii* at Low Temperatures. *Eur. Biophys. J.* **1999**, *28*, 243−253.
(37) Vulto, S. I. E.; de Baat, M. A.; Neerken, S.; Nowak, F. R.; van Amerongen, H.; Amesz, J.; Aartsma, T. J. Excited State Dynamics in FMO Antenna Complexes from Photosynthetic Green Sulfur Bacteria: A Kinetic Model. *J. Phys. Chem. B* **1999**, *103*, 8153−8161.
(38) Wendling, M.; Przyjalgowski, M. A.; Gülen, D.; Vulto, S. I. E.; Aartsma, T. J.; Grondelle, R. v.; Amerongen, H. v. The Quantitative Relationship between Structure and Polarized Spectroscopy in the FMO Complex of *Prosthecochloris aestuarii*: Refining Experiments and Simulations. *Photosynth. Res.* **2002**, *71*, 99−123.
(39) Adolphs, J.; Renger, T. How Proteins Trigger Excitation Energy Transfer in the FMO Complex of Green Sulfur Bacteria. *Biophys. J.* **2006**, *91*, 2778−2797.
(40) Read, E. L.; Schlau-Cohen, G. S.; Engel, G. S.; Wen, J.; Blankenship, R. E.; Fleming, G. R. Visualization of Excitonic Structure in the Fenna-Matthews-Olson Photosynthetic Complex by Polarization-Dependent Two-Dimensional Electronic Spectroscopy. *Biophys. J.* **2008**, *95*, 847−856.
(41) Schmidt am Busch, M.; Müh, F.; El-Amine Madjet, M.; Renger, T. The Eighth Bacteriochlorophyll Completes the Excitation Energy Funnel in the FMO Protein. *J. Phys. Chem. Lett.* **2011**, *2*, 93−98.
(42) Gao, J.; Shi, W.-J.; Ye, J.; Wang, X.; Hirao, H.; Zhao, Y. QM/MM Modeling of Environmental Effects on Electronic Transitions of the FMO Complex. *J. Phys. Chem. B* **2013**, *117*, 3488−3495.
(43) List, N. H.; Curutchet, C.; Knecht, S.; Mennucci, B.; Kongsted, J. Toward Reliable Prediction of the Energy Ladder in Multi-chromophoric Systems: A Benchmark Study on the FMO Light-Harvesting Complex. *J. Chem. Theory Comput.* **2013**, *9*, 4928−4938.
(44) Saer, R. G.; Stadnytskyi, V.; Magdaong, N. C.; Goodson, C.; Savikhin, S.; Blankenship, R. E. Probing the Excitonic Landscape of the *Chlorobaculum tepidum* Fenna-Matthews-Olson (FMO) Complex: a Mutagenesis Approach. *Biochim. Biophys. Acta* **2017**, *1858*, 288−296.
(45) Olbrich, C.; Jansen, T. L. C.; Liebers, J.; Aghtar, M.; Strümpfer, J.; Schulten, K.; Knoester, J.; Kleinekathöfer, U. From Atomistic Modeling to Excitation Transfer and Two-Dimensional Spectra of the FMO Light-Harvesting Complex. *J. Phys. Chem. B* **2011**, *115*, 8609−8621.
(46) Chandrasekaran, S.; Aghtar, M.; Valleau, S.; Aspuru-Guzik, A.; Kleinekathöfer, U. Influence of Force Fields and Quantum Chemistry Approach on Spectral Densities of BChl a in Solution and in FMO Proteins. *J. Phys. Chem. B* **2015**, *119*, 9995−10004.
(47) Wendling, M.; Pullerits, T.; Przyjalgowski, M. A.; Vulto, S. I. E.; Aartsma, T. J.; van Grondelle, R.; van Amerongen, H. Electron-Vibrational Coupling in the Fenna-Matthews-Olson Complex of *Prosthecochloris aestuarii* Determined by Temperature-Dependent

Absorption and Fluorescence Line-Narrowing Measurements. *J. Phys. Chem. B* **2000**, *104*, 5825−5831.
(48) Tanimura, Y. Stochastic Liouville, Langevin, Fokker−Planck, and Master Equation Approaches to Quantum Dissipative Systems. *J. Phys. Soc. Jpn.* **2006**, *75*, 082001.
(49) Kubo, R.; Toda, M.; Hashitsume, N. *Statistical Physics II: Nonequilibrium Statistical Mechanics*; Springer-Verlag Berlin Heidelberg: 1991.
(50) Jansen, T. l. C.; Knoester, J. Nonadiabatic Effects in the Two-Dimensional Infrared Spectra of Peptides: Application to Alanine Dipeptide. *J. Phys. Chem. B* **2006**, *110*, 22910−22916.
(51) Ma, J.; Cao, J. Förster resonance energy transfer, absorption and emission spectra in multichromophoric systems. I. Full cumulant expansions and system-bath entanglement. *J. Chem. Phys.* **2015**, *142*, 094106.
(52) Strümpfer, J.; Schulten, K. Open Quantum Dynamics Calculations with the Hierarchy Equations of Motion on Parallel Computers. *J. Chem. Theory Comput.* **2012**, *8*, 2808−2816.
(53) Ishizaki, A.; Fleming, G. R. Theoretical Examination of Quantum Coherence in a Photosynthetic System at Physiological Temperature. *Proc. Natl. Acad. Sci. U.S.A.* **2009**, *106*, 17255−17260.
(54) Huo, P.; Coker, D. F. Iterative Linearized Density Matrix Propagation for Modeling Coherent Excitation Energy Transfer in Photosynthetic Light Harvesting. *J. Chem. Phys.* **2010**, *133*, 184108.
(55) Tao, G.; Miller, W. H. Semiclassical Description of Electronic Excitation Population Transfer in a Model Photosynthetic System. *J. Phys. Chem. Lett.* **2010**, *1*, 891−894.
(56) Kelly, A.; Rhee, Y. M. Mixed Quantum-Classical Description of Excitation Energy Transfer in a Model Fenna-Matthews-Olsen Complex. *J. Phys. Chem. Lett.* **2011**, *2*, 808−812.
(57) Moix, J.; Wu, J.; Huo, P.; Coker, D.; Cao, J. Efficient Energy Transfer in Light-Harvesting Systems, III: The Influence of the Eighth Bacteriochlorophyll on the Dynamics and Efficiency in FMO. *J. Phys. Chem. Lett.* **2011**, *2*, 3045−3052.
(58) Ritschel, G.; Roden, J.; Strunz, W. T.; Aspuru-Guzik, A.; Eisfeld, A. Absence of Quantum Oscillations and Dependence on Site Energies in Electronic Excitation Transfer in the Fenna-Matthews-Olson Trimer. *J. Phys. Chem. Lett.* **2011**, *2*, 2912−2917.
(59) Zhu, J.; Kais, S.; Rebentrost, P.; Aspuru-Guzik, A. Modified Scaled Hierarchical Equation of Motion Approach for the Study of Quantum Coherence in Photosynthetic Complexes. *J. Phys. Chem. B* **2011**, *115*, 1531−1537.
(60) Renaud, N.; Ratner, M. A.; Mujica, V. A Stochastic Surrogate Hamiltonian Approach of Coherent and Incoherent Exciton Transport in the Fenna-Matthews-Olson Complex. *J. Chem. Phys.* **2011**, *135*, 075102.
(61) Mohseni, M.; Rebentrost, P.; Lloyd, S.; Aspuru-Guzik, A. Environment-Assisted Quantum Walks in Photosynthetic Energy Transfer. *J. Chem. Phys.* **2008**, *129*, 174106.
(62) Rebentrost, P.; Mohseni, M.; Kassal, I.; Lloyd, S.; Aspuru-Guzik, A. Environment-assisted quantum transport. *New. J. Phys.* **2009**, *11*, 033003.
(63) Wu, J.; Liu, F.; Shen, Y.; Cao, J.; Silbey, R. J. Efficient Energy Transfer in Light-Harvesting Systems, I: Optimal Temperature, Reorganization Energy and Spatial-Temporal Correlations. *New J. Phys.* **2010**, *12*, 105012.
(64) Ishizaki, A.; Fleming, G. R. On the Adequacy of the Redfield Equation and Related Approaches to the Study of Quantum Dynamics in Electronic Energy Transfer. *J. Chem. Phys.* **2009**, *130*, 234110.
(65) Ishizaki, A.; Fleming, G. R. Unified Treatment of Quantum Coherent and Incoherent Hopping Dynamics in Electronic Energy Transfer: Reduced Hierarchy Equation Approach. *J. Chem. Phys.* **2009**, *130*, 234111.
(66) Plenio, M. B.; Huelga, S. F. Dephasing-Assisted Transport: Quantum Networks and Biomolecules. *New J. Phys.* **2008**, *10*, 113019.
(67) Dutta, R.; Bagchi, B. Effects of Dynamic Disorder on Exciton Migration: Quantum Diffusion, Coherences, and Energy Transfer. *J. Chem. Phys.* **2016**, *145*, 164907.
(68) Otte, S. C. M.; van der Heiden, J. C.; Pfennig, N.; Amesz, J. A comparative study of the optical characteristics of intact cells of photosynthetic green sulfur bacteria containing bacteriochlorophyll c, d or e. *Photosynth. Res.* **1991**, *28*, 77−87.
(69) Dostál, J.; Pšenčík, J.; Zigmantas, D. In situ mapping of the energy flow through the entire photosynthetic apparatus. *Nat. Chem.* **2016**, *8*, 705−710.
(70) Womick, J. M.; Moran, A. M. Vibronic enhancement of exciton sizes and energy transport in photosynthetic complexes. *J. Phys. Chem. B* **2011**, *115*, 1347−1356.
(71) Turner, D. B.; Wilk, K. E.; Curmi, P. M. G.; Scholes, G. D. Comparison of Electronic and Vibrational Coherence Measured by Two-Dimensional Electronic Spectroscopy. *J. Phys. Chem. Lett.* **2011**, *2*, 1904−1911.
(72) Christensson, N.; Kauffmann, H. F.; Pullerits, T.; Mančal, T. Origin of long-lived coherences in light-harvesting complexes. *J. Phys. Chem. B* **2012**, *116*, 7449−7454.
(73) Kreisbeck, C.; Kramer, T. Long-Lived Electronic Coherence in Dissipative Exciton Dynamics of Light-Harvesting Complexes. *J. Phys. Chem. Lett.* **2012**, *3*, 2828−2833.
(74) Nalbach, P.; Mujica-Martinez, C. A.; Thorwart, M. Vibronically coherent speed-up of the excitation energy transfer in the Fenna-Matthews-Olson complex. *Phys. Rev. E: Stat., Nonlinear, Soft Matter Phys.* **2015**, *91*, 022706.
(75) Fujihashi, Y.; Fleming, G. R.; Ishizaki, A. Impact of Environmentally Induced Fluctuations on Quantum Mechanically Mixed Electronic and Vibrational Pigment States in Photosynthetic Energy Transfer and 2D Electronic Spectra. *J. Chem. Phys.* **2015**, *142*, 212403.
(76) Liu, X.; Kühn, O. Vibrational and vibronic coherences in the dynamics of the FMO complex. *Chem. Phys.* **2016**, *481*, 272−280.
(77) Romero, E.; Novoderezhkin, V. I.; van Grondelle, R. Quantum design of photosynthesis for bio-inspired solar-energy conversion. *Nature* **2017**, *543*, 355−365.